Journal of Natural Gas Science and Engineering 34 (2016) 948–957

Contents lists available at ScienceDirect

Journal of Natural Gas Science and Engineering

journal homepage: www.elsevier.com/locate/jngse

Pore-scale geometry effects on gas permeability in shale

Ziyan Wang [a], Xu Jin [b, c], Xiaoqi Wang [b, c], Liang Sun [b, c], Moran Wang [a, *]

[a] Department of Engineering Mechanics and CNMM, Tsinghua University, Beijing 100084, China
[b] Petroleum Geology Research & Laboratory Center, Research Institute of Petroleum Exploration & Development (RIPED) PetroChina, Beijing 100083, China
[c] National Energy Tight Oil & Gas Research Centre, Beijing 100083, China

ARTICLE INFO

Article history:
Received 1 June 2016
Received in revised form
19 July 2016
Accepted 23 July 2016
Available online 28 July 2016

Keywords:
Shale gas
Anisotropy and heterogeneity
Knudsen number
Geometry effect
Lattice Boltzmann method

ABSTRACT

One main challenge for prediction of gas permeability in shale is the geometrical complexity at pore scale of shale. Shale structure is highly anisotropic and heterogeneous, which cannot be well described by packing of spheres or bundle of tubes. Besides, there are abundant nanoscale pores in shale so that the Knudsen number of gas flow is high, leading to failure of the conventional Darcy's law. Aiming at these challenges, we have studied the influences from pore-scale anisotropy and heterogeneity of shale microstructures on gas permeability including the high Knudsen number effect (or Klinkenberg effect for Darcy scale). First, a geometry-based method is proposed to quantify the pore-scale anisotropy and heterogeneity of shale. Then we reconstruct three-dimensional shale structures by the random generation-growth algorithm and use the lattice Boltzmann method to predict its permeability. To reveal the high Knudsen number effect, both intrinsic permeability and apparent permeability are evaluated. Our results suggest that the intrinsic permeability increases with the anisotropy of pore geometry in parallel direction to the bed, while decreases in perpendicular direction. The slip factor for Klinkenberg correction also exhibits anisotropy when high Knudsen effect is considered. On the other hand, the heterogeneity of pore distribution may have positive influences on intrinsic permeability for given porosities.

1. Introduction

With the declination of conventional natural gas resources, shale gas becomes more and more important because of its huge storage and relatively matured exploitation technology. To optimize the exploitation and predict the gas production, the gas permeability of shale is an important parameter. However, there is no precise model for shale gas permeability yet, because shale has very complex geometry for gas transports. Generally, shale structure is highly anisotropic and heterogeneous, and most organic pores are at nanoscale. A quantitative description of these features and their influences on gas flow is essential for shale permeability modeling.

Experiments have shown that shale is strongly anisotropic and the permeability parallel to the bed is one, or more, order of magnitude higher than the perpendicular permeability (Kwon et al., 2004). The anisotropy of shale is reflected at both macro scale and pore scale. At macro scale, shale has layered structure, which has been studied and modeled by many researchers. Begg and Chang (1985) developed a statistical method to predict the perpendicular permeability of reservoir containing discontinuous plate-like shales. McCarthy (1991) considered the flow in layered sandstone-shale structure by both analytical modeling and numerical simulation. Burton and Wood (2013) provided quantitative characteristic data of the layered shale morphology and studied its influence on permeability. Besides, the anisotropy of shale is also observed at pore scale, for example, the structure of organic matter is anisotropic too. As shown by micro scanning, some organic pores in shale have large aspect ratio (Kwon et al., 2004) and the geometry parallel or perpendicular to the bed direction is quite different (Wan et al., 2015). This kind of anisotropy has been quantitatively characterized through neutron scattering by Gu et al. (2015), which, however, contains scattering intensity limiting the application as a result. A geometry-based definition of pore-scale anisotropy is desired and the relation to permeability is in demand.

The heterogeneity of shale exists at two scales as well. At macro scale, there are many material compositions in shale, such as kerogen, pyrites, clay and calcite (Loucks et al., 2009). Each composition has its own characteristic morphology and it is very

* Corresponding author.
E-mail address: mrwang@tsinghua.edu.cn (M. Wang).

http://dx.doi.org/10.1016/j.jngse.2016.07.057
1875-5100/

difficult, if not impossible, to describe them in a unified model. The heterogeneity at pore scale refers to the non-uniform distribution of pores, which is clearly presented in many observations (Tang et al., 2015; Lin et al., 2015). Recently, some pore-scale models have considered the heterogeneous pore distribution, such as the pore-network modeling by Zhang et al. (2015) and lattice Boltzmann simulation by Chen et al. (2015). However, in these works the pore-scale heterogeneity was not quantified and therefore its influence has not been explained yet.

The third feature of shale geometry is that nanoscale pores are dominant (Chalmers et al., 2012). When pore size is comparable to the mean free path of gas molecules, the Knudsen number (Kn) becomes high and the gas permeability is no longer a constant (Karniadakis et al., 2005; Wang et al., 2008). Starting from Klinkenberg (1941), many models have been proposed regarding to the high Kn effect in porous flow (Civan, 2010). However most models are built for isotropic and homogeneous structures. When anisotropy is concerned, some works assume that the slip factor in Klinkenberg correction remains isotropic (Kaluarachchi, 1995; Shmonov et al., 2011), while recent experiments show that in graphite compression packings, the intrinsic permeability and slip factor are both highly anisotropic (Lasseux et al., 2011). It is very important and valuable to make clear whether the anisotropy of shale microstructure can enhance the high Kn effect or not.

In this work, we focus on the pore-scale anisotropy and heterogeneity, because macroscale anisotropy has been well-studied and the heterogeneity in macroscale is too complex to describe in a unified model. For simplicity, **we refer anisotropy and heterogeneity in particular to the pore-scale anisotropy and heterogeneity in below**. Both intrinsic and apparent permeability are studied to reflect the high Kn effect. We firstly develop a geometry-based method to quantify the anisotropy and heterogeneity and apply it to the micro scanning images of shale. Then, according to the quantified results, we reconstruct 3D shale structure based on Quartet Structure Generation Set (QSGS) method. Finally, the intrinsic permeability and apparent permeability are predicted by lattice Boltzmann method (LBM) and a quantitative relationship between geometry features and gas permeability is established.

2. Quantification of anisotropy and heterogeneity

2.1. Anisotropy

Because of the compaction in vertical direction, most shale has a transversely isotropic structure (Wang, 2002). This means that shale is isotropic in any direction parallel to the bed and the anisotropy only appears in the plane perpendicular to bed. As the formation process of shale is various, the anisotropy of pore structure is also different. Fig. 1 shows the varied pore geometry in the organic matters of shale.

To quantify the anisotropy, we firstly extract the pore geometry from shale image (take Fig. 1 (c) for example, as shown in Fig. 2). Then we consider a line crossing the structure along the bed and define the average pore number it can encounter per unit length as n_x. Similarly we can define n_y in the direction perpendicular to the bed. The anisotropy of the pore structure is defined as

$$A = \frac{n_y}{n_x}. \tag{1}$$

The quantified anisotropy of the 4 structures in Fig. 1 is shown in Table 1. It should be noted that although illustrated by 2D image, this definition is also suitable for 3D structure.

The defined anisotropy can reflect the aspect ratio of the pores, which is explained in details in Appendix A. As a simple illustration, we consider a specific case that all pores are elliptical with the same eccentricity and same orientation along x direction (the pore size can be varied). The anisotropy of the structure equals a/b, where a is the semi-major axis and b is the semi-minor axis, which is in agreement with common sense. There are mainly two advantages in this quantification method. First, it is purely geometry based and physical parameters, such as scattering intensity, are not included. Second, it is not affected by the non-uniform distribution of pores, which is necessary to study anisotropy and heterogeneity separately.

2.2. Heterogeneity

Before quantification, we need to clarify that the heterogeneity is depended on the observation scale. For example, if the observation scale is less than pore diameter, all porous structures are heterogeneous because the difference of pore and solid. On the other hand, if the observation scale is larger than the scale of representative elementary volume (REV), all porous structures are homogeneous. Thus, we firstly define the observation scale l_x, l_y, l_z along x, y, z direction respectively. After that, we divide the whole porous structure into blocks with side length of l_x, l_y, l_z. Then we use the relative standard deviation of each block's porosity to quantify the heterogeneity of pore distribution:

$$H = \frac{1}{\phi}\sqrt{\frac{\sum(\phi_i - \phi)^2}{n-1}} \tag{2}$$

where ϕ_i is the porosity of i-th block and ϕ is the total porosity. For 2D case, only two observation scales are required and the expression for heterogeneity is the same.

To demonstrate the heterogeneity of pore distribution in shale, we consider 4 images cutting parallel to bed, as shown in Fig. 3. After extracting the pore geometry, each image is divided into 4×4 blocks (Fig. 4) and the quantified heterogeneity is presented in Table 1. Just as before, the quantification of heterogeneity is geometry based and not affected by anisotropy, so the anisotropy and heterogeneity are studied separately in the following sections.

3. Structure reconstruction

For real shale samples, the properties such as porosity, anisotropy and heterogeneity are all varied. But to study the influence from a specific factor, all other parameters must be kept constant. Thus, direct simulation in real structure is not appropriate when we want to reveal the geometry effect on permeability. In contrast, structure reconstructed by statistical method has adjustable properties, while the morphology is consistent with real samples. Thus, we adopt the QSGS algorithm (Wang et al., 2007a; Wang and Pan, 2008) to reconstruct the porous structure, which is described as follows.

(1) Randomly generate cores in a grid system according to the core distribution probability c, i.e. each cell in the grid system has the probability c to become solid.
(2) Expand every solid element to its neighboring cell in normal directions based on the growth rate D_x, D_y, D_z in x, y, z directions respectively.
(3) Repeat step (2) until the porosity is reduced to the desired value ε.

The anisotropy of the structure can be realized by varying the growth rate in different directions. Since shale has transversely isotropic geometry, we choose $D_z < D_x = D_y$ and an example structure with $D_x/D_z = 7$ is presented in Fig. 5 (a).

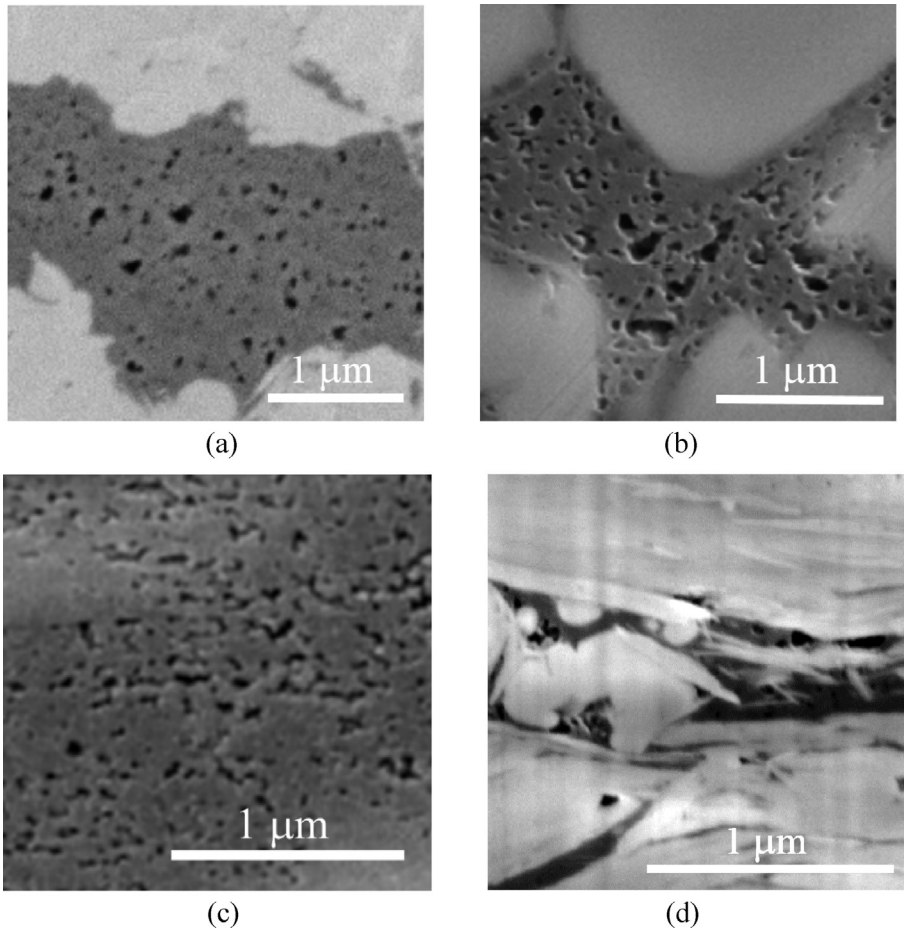

Fig. 1. Different pore geometry in the organic matters of shale. The black represents the organic nanopores while the dark grey is the organic matter and the light grey is the mineral matrix. The cutting direction is perpendicular to the bed and the samples are from different regions: (a) Longmaxi, China (obtained by our own SEM scanning); (b) Barnett, USA (Bhandari et al., 2015); (c) Niutitang, China (Wan et al., 2015); (d) Marcellus, USA (Gu et al., 2015).

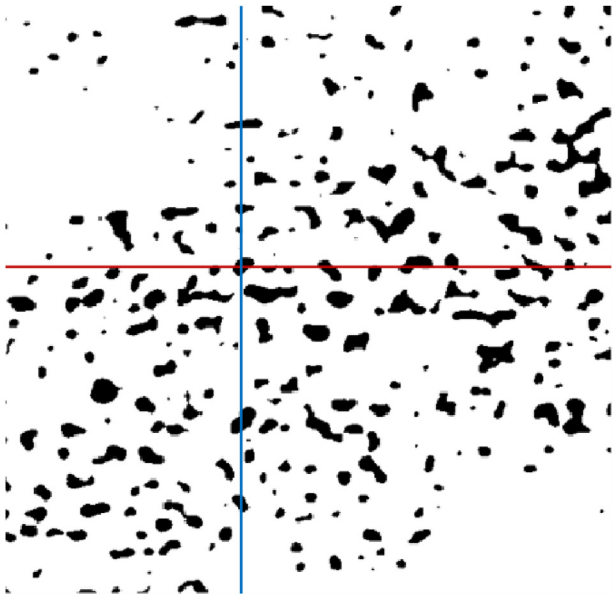

Fig. 2. The pore geometry extracted from shale image in Fig. 1 (c), with pores represented by black and matrix by white. The average pore number encountered by the red and blue lines is used to quantify the anisotropy. (For interpretation of the references to colour in this figure legend, the reader is referred to the web version of this article.)

Table 1
The anisotropy and heterogeneity of shale image in Figs. 1 and 4, respectively.

Anisotropic structure		Heterogeneous structure	
Geometry in Fig. 1	Anisotropy, A	Geometry in Fig. 4	Heterogeneity, H
(a)	0.979	(a)	0.678
(b)	1.156	(b)	0.876
(c)	1.253	(c)	1.218
(d)	1.607	(d)	1.756

The heterogeneity cannot be accomplished by original QSGS algorithm and we propose a two-scale generation method to realize it.

(i) Create a refined structure with core distribution probability c^R, growth rate $D^R{}_x$, $D^R{}_y$, $D^R{}_z$ and porosity ε^R.
(ii) Independently construct another coarse structure: generate cores with distribution probability $c^C \ll c^R$ and expand with growth rate $D^C{}_x$, $D^C{}_y$, $D^C{}_z$.
(iii) The final structure is the combination of the refined structure and the coarse structure, i.e. the cell is solid if it is occupied by either of the structures. When the combined structure reaches the desired porosity ε, stop growing the coarse structure.

In the two-scale scheme, the refined structure represents the subtle geometry of organic matter, while the coarse structure

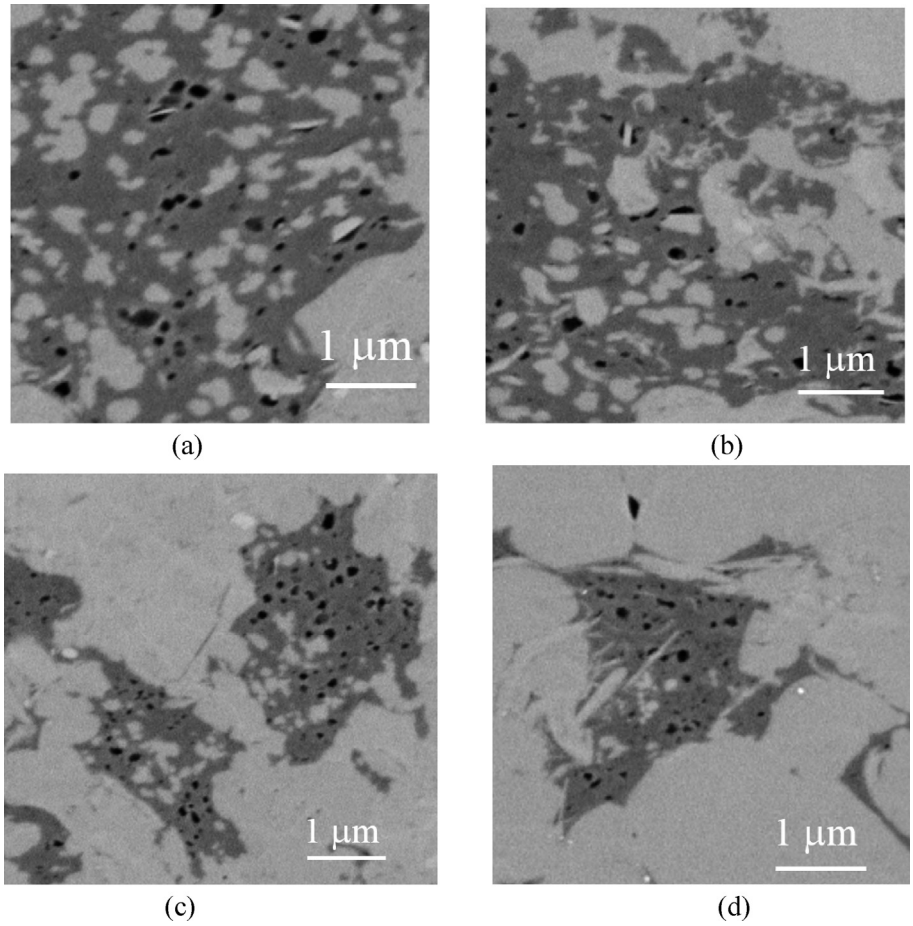

Fig. 3. The shale images showing the heterogeneous pore distribution. The black represents the organic nanopores while the dark grey is the organic matter and the light grey is the mineral matrix. The cut direction is parallel to the bed and the samples are taken from Longmaxi shale, China (obtained by our own SEM scanning).

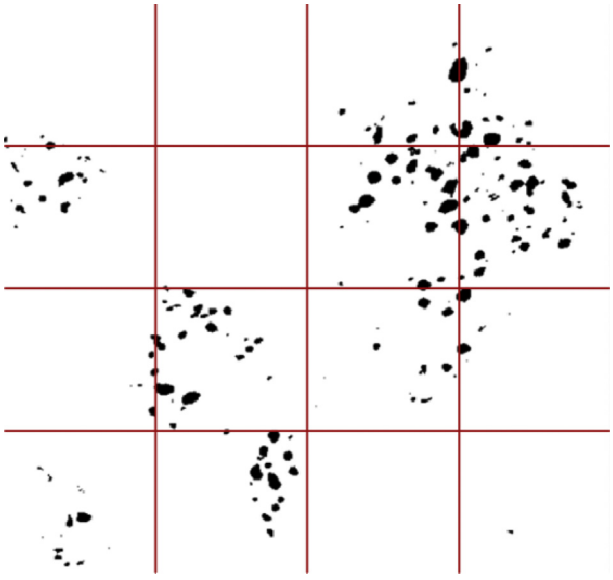

Fig. 4. The heterogeneous pore geometry extracted from Fig. 3 (c), with pores represented by black and matrix by white. The image is uniformly divided into 4 × 4 blocks by the red lines when quantifying the heterogeneity. (For interpretation of the references to colour in this figure legend, the reader is referred to the web version of this article.)

represents the mineral matrix. The structure heterogeneity is positively related with c^R/c^C and an example structure with $c^R/c^C = 250$ is presented in Fig. 5 (b). In this work, we take the same value for the six growth rates in the two structures, but they can be set different to couple the heterogeneity and anisotropy.

4. Simulation method

The lattice Boltzmann method (LBM) is applied to simulate the isothermal flow in reconstructed porous media. LBM has high efficiency in dealing with complex wall boundary (Wang and Chen, 2007; Wang et al., 2007b), which is the main challenge for porous flow simulation. Besides, LBM is derived directly from Boltzmann equation (Chen and Doolen, 1998; He and Luo, 1997) so it has a solid physical foundation, especially when high *Kn* effect is concerned. LBM discretizes the distribution function and describes its evolution:

$$f_i(\mathbf{x} + \mathbf{c}_i\Delta t, t + \Delta t) - f_i(\mathbf{x}, t) = \Omega_i(f), \quad i = 0, 1, \cdots, N-1 \qquad (3)$$

where f_i ($\mathbf{x}$, t) is the discrete distribution function; $\mathbf{c}_i$ is the lattice speed; $\Omega_i(f)$ is the discrete collision operator and N is the number of the discrete velocities. The lattice speed model D3Q19 (3 dimension 19 speed) is used in this work for numerical accuracy (Wang and Kang, 2009). As for the collision operator, we adopt the multiple relaxation time model (MRT) (Higuera et al., 1989; Lallemand and Luo, 2000) because of its good stability for complex geometry (d'Humieres et al., 2002; Pan et al., 2006). The MRT model is

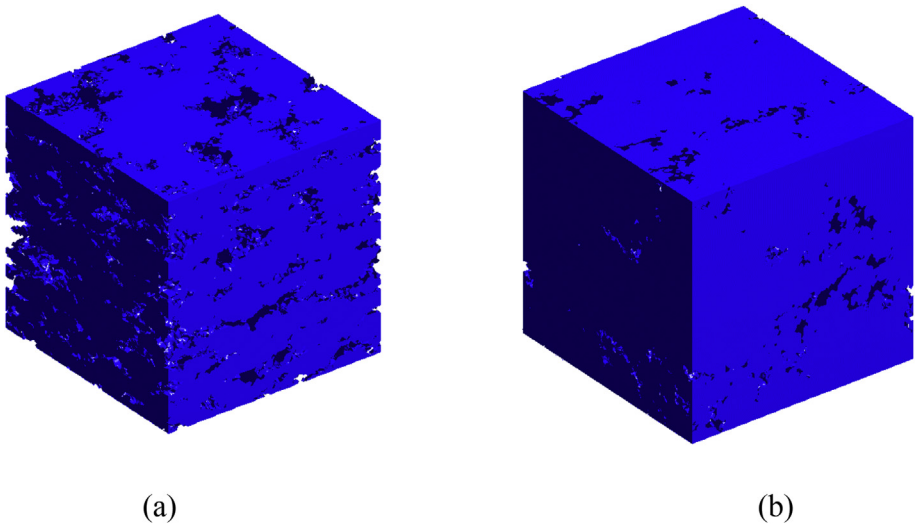

Fig. 5. Two example structures reconstructed based on QSGS method: (a) anisotropic structure with $D_x/D_z = 7$; (b) heterogeneous structure with $c^R/c^C = 250$.

expressed as:

$$\Omega_i = -\sum_j \left(\mathbf{M}^{-1}\mathbf{S}\mathbf{M}\right)_{ij}\left(f_j - f_j^{eq}\right), \tag{4}$$

where **M** is a 19 × 19 matrix, whose value was given by d'Humieres et al., (2002). **S** is a diagonal matrix (Pan et al., 2006):

$$\mathbf{S} = \mathrm{diag}\left(0, s_e, s_\varepsilon, 0, s_q, 0, s_q, 0, s_q, s_v, s_\pi, s_v, s_\pi, s_v, s_v, s_v, s_m, s_m, s_m\right), \tag{5}$$

$$s_v = \frac{1}{\tau}, \quad s_e = s_\varepsilon = s_\pi = s_m = s_q = 8\frac{2 - s_v}{8 - s_v}, \tag{6}$$

where τ is the relaxation time given later by Eq. (9). The f_i^{eq} in Eq. (4) is the equilibrium distribution function with the form of

$$f_i^{eq} = \omega_i \rho\left[1 + \frac{\mathbf{c}_i \cdot \mathbf{u}}{RT} + \frac{(\mathbf{c}_i \cdot \mathbf{u})^2}{2(RT)^2} + \frac{\mathbf{u} \cdot \mathbf{u}}{2RT}\right], \tag{7}$$

where ω_i is the weight of direction i in D3Q19 model; R is the specific gas constant and T is the temperature. The variables ρ and **u** are local density and velocity respectively, determined by the discrete distribution function:

$$\rho = \sum_i f_i, \quad \mathbf{u} = \frac{1}{\rho}\sum_i \mathbf{c}_i f_i. \tag{8}$$

Eq. (8) also links the distribution function in LBM to the physical quantities.

For the boundary conditions, we apply the pressure boundary at inlet and outlet and periodic boundary in the other two directions (Guo et al., 2002). The pressure difference is very small so that the variation of gas properties is negligible. As for wall boundary, since the generated structure already has a zigzag interface, the classical LBM wall boundary can be directly applied. We adopt the bounce-back scheme for non-slip flow and diffusive wall boundary for high *Kn* flow.

To verify the numerical method, the steady-state non-slip flow through packed spheres is studied. The spheres are arranged in body centered cubic (BCC) array with porosity of 0.582 and side length of 320 nm (Fig. 6 (a)). We compare the stability of MRT model against the single relaxation time (SRT) model in Fig. 6 (b). Similar as reported by Pan et al. (2006), The SRT result for intrinsic permeability is strongly dependent on relaxation time:

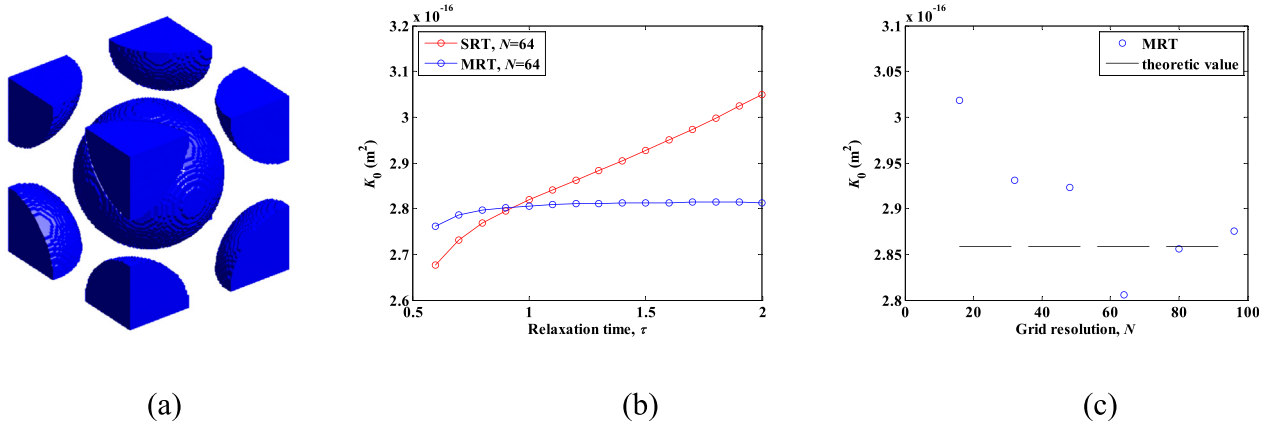

Fig. 6. The LBM simulation for intrinsic permeability K_0 of BCC structure: (a) The simulation structure with grid resolution $N = 96$; (b) The stability test for SRT and MRT model; (c) The comparison of MRT result to theoretic value from Sangani and Acrivos (1982).

Table 2
The parameters for reconstructed structure in simulation.

Anisotropic structure		Heterogeneous structure	
Core distribution probability, c	0.01	Core distribution probability for refined structure, c^R	0.01
		Core distribution probability for coarse structure, c^C	1×10^{-4}, 8×10^{-5}, 6×10^{-5}, 4×10^{-5}, 2×10^{-5},
Porosity, ε	0.3	Porosity for refined structure, ε^R	0.3
		Porosity, ε	0.1
Grid resolution	$30 \times 100 \times 100$	Grid resolution	$30 \times 100 \times 100$
Cell scale (nm)	20	Cell scale (nm)	20
Growth rate along x, D_x	0.008	Growth rate	0.008
Growth rate along y, D_y	0.008		
Growth rate ratio, D_x/D_z	1, 3, 5, 7, 9		

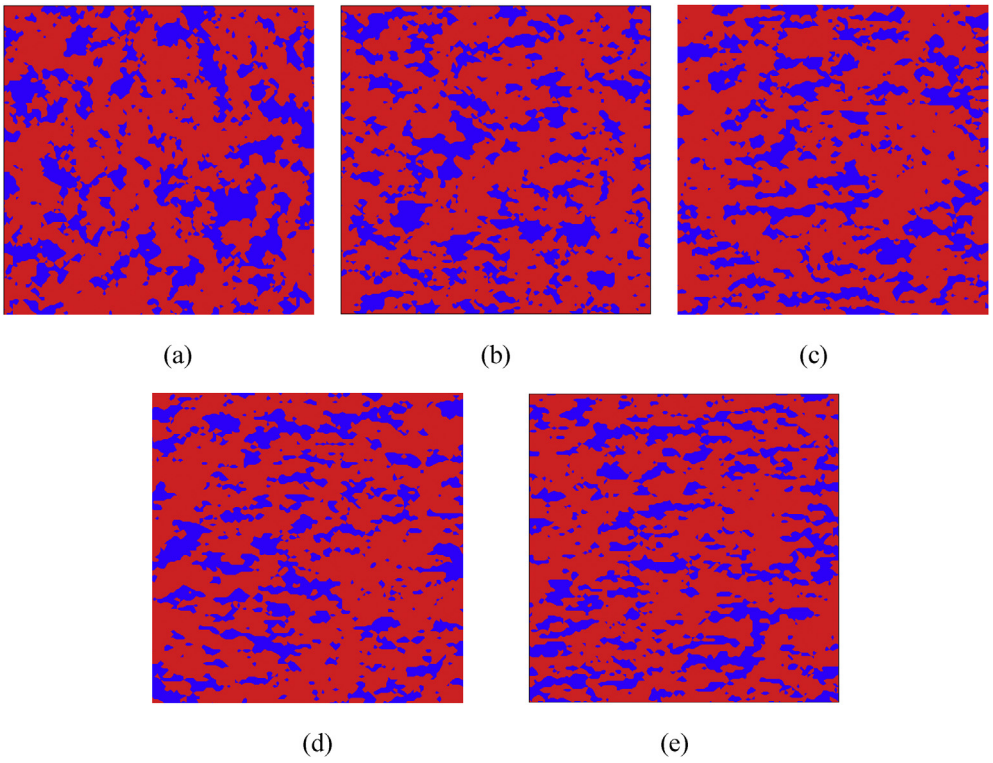

Fig. 7. The cross section perpendicular to the flow direction (x direction) of one group of the reconstructed anisotropic structures, with pores represented by blue and matrix by red. The growth rate ratio from (a) to (e) is 1, 3, 5, 7, 9, respectively. (For interpretation of the references to colour in this figure legend, the reader is referred to the web version of this article.)

Table 3
The average anisotropy and heterogeneity for structures in simulation.

Anisotropic structure		Heterogeneous structure	
Growth rate ratio, D_x/D_z	Average anisotropy, A	Core distribution probability ratio, c^R/c^C	Average heterogeneity, H
1	1.00	100	0.737
3	1.29	125	0.783
5	1.45	167	0.863
7	1.57	250	0.889
9	1.67	500	1.05

$$\tau = \frac{1}{2} + \frac{\mu}{\rho \Delta x}\sqrt{\frac{3}{RT}}, \tag{9}$$

where μ is the dynamic gas viscosity and Δx is the lattice length. Since the relaxation time is determined by gas properties when the lattice is settled, it means the intrinsic permeability is affected by gas properties in SRT model, which is physically incorrect. In contrast, MRT model shows good stability with the variation of relaxation time, thus it is adopted in our simulation. The MRT result is also compared with the analytical solution of Sangani and Acrivos (1982) in Fig. 6 (c). With the increasing of grid resolution, the error decreases in general. The error is mainly introduced by the discretion of the sphere since its radius could be a little lower or higher than the desired value. But even with the lowest grid resolution with just 16 cells per side, the error is only about 5 percent, which reflects the accuracy of LBM and its advantage for low resolution grid.

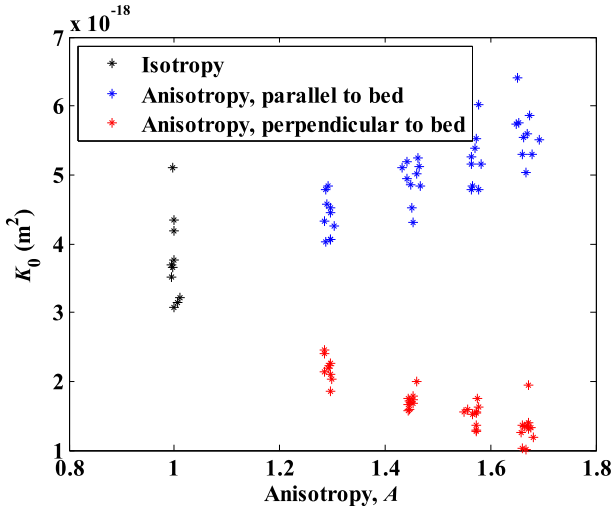

Fig. 8. The intrinsic permeability of structures having different anisotropy, with each point reprenting the permeability of a reconstructed structure. The intrinsic permeability of isotropic structures (black points), anisotropic structures in parallel direction (blue points) and perpendicular direction (red points) are presented. (For interpretation of the references to colour in this figure legend, the reader is referred to the web version of this article.)

To consider the high *Kn* flow, *Kn* is firstly defined for porous media (Knudsen, 1933):

$$Kn = \frac{\lambda}{l}, \tag{10}$$

where λ is the mean free path of the gas molecules; l is the characteristic length (Civan, 2010):

$$l = \frac{2V_p}{S}, \tag{11}$$

where V_p is the pore volume and S is the interface area between pore and solid.

The high *Kn* effect is realized by introducing the diffusive wall boundary based on kinetic theory and the effective viscosity. Based on the work of Ansumali and Karlin (2002), a general form of diffusive boundary, which is applicable for both channel and porous media, is expressed as:

$$f_i^{new} = \frac{\omega_i}{\sum_{j,\text{solid}} \omega_j} \sum_{j,\text{solid}} f_j, \tag{12}$$

where i is the direction in which the distribution function is unknown; j is the direction pointing to solid cell. Another characteristic for high *Kn* flow is that the molecular movement is confined by the structure, leading to a lower effective mean free path and thus lower effective viscosity than the bulk. The Bosanquet-type viscosity model is applied in this work:

$$\mu_e = \frac{\mu}{1 + aKn}, \tag{13}$$

where $a = 2.2$ suggested by Beskok and Karniadakis (1999). The accuracy of the above LBM scheme for high *Kn* flow has been proved in our previous work (Wang et al., 2016). It should be noted that $a = 2.2$ is strictly valid for channel with length-height ratio of 20. Kalarakis et al. (2012) found that for two-dimensional porous flow, the value of a is about 3.4–4, but they suggest the error caused by a is acceptable for porous flow. For simplicity, we adopt $a = 2.2$ to evaluate the high *Kn* effect in the three-dimensional porous structure. If more precise results are desired, a should be determined by fitting the experimental data.

5. Results

The flow in anisotropic structure and heterogeneous structure is simulated separately in this section. For each value of anisotropy or heterogeneity, ten structures are created and simulated to reduce the error caused by random growth algorithm. Both intrinsic and apparent permeability are predicted by simulation and the slip factor is calculated to evaluate the high *Kn* effect.

5.1. Anisotropy

The parameters in the structure reconstruction are presented in Table 2. A grid system with the resolution of 30 × 100 × 100 is chosen so that the flow has a larger cross section and the fluctuation can be reduced. Fig. 7 shows the cross section of the structure with growth rate ratio from 1 to 9 and the corresponding anisotropy (average of 10 structures) is presented in Table 3. Compared with Fig. 1 and Table 1, the anisotropy of real shale and reconstructed structure is at the same level and the pore morphology is similar, proving that the reconstructed structure can reflect the properties of real shale. In our simulation, we further conduct a grid refinement which doubled the grid number in each side, so the final grid resolution is 60 × 200 × 200 with 10 nm cell scale.

We firstly simulate the steady-state non-slip flow by LBM to determine the intrinsic permeability. Without loss of generality, the gas pressure is adjusted so that the relaxation time is kept to 1. For the anisotropic structures described above, the flow direction is

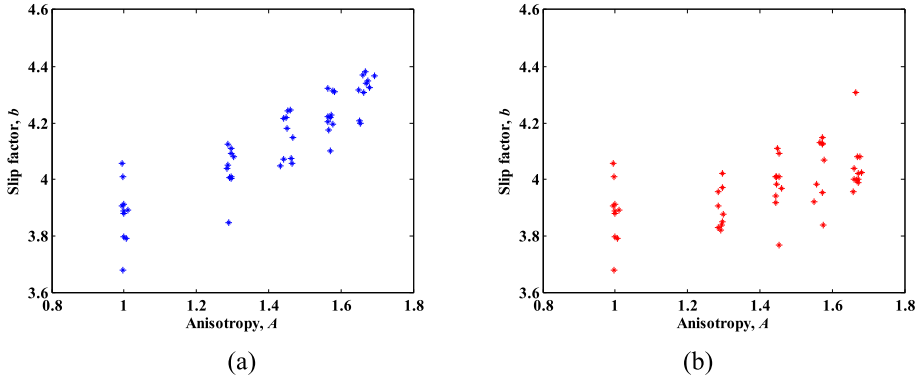

Fig. 9. The slip factor for anisotropic structures, with flow direction parallel to bed (a) and perpendicular to bed (b).

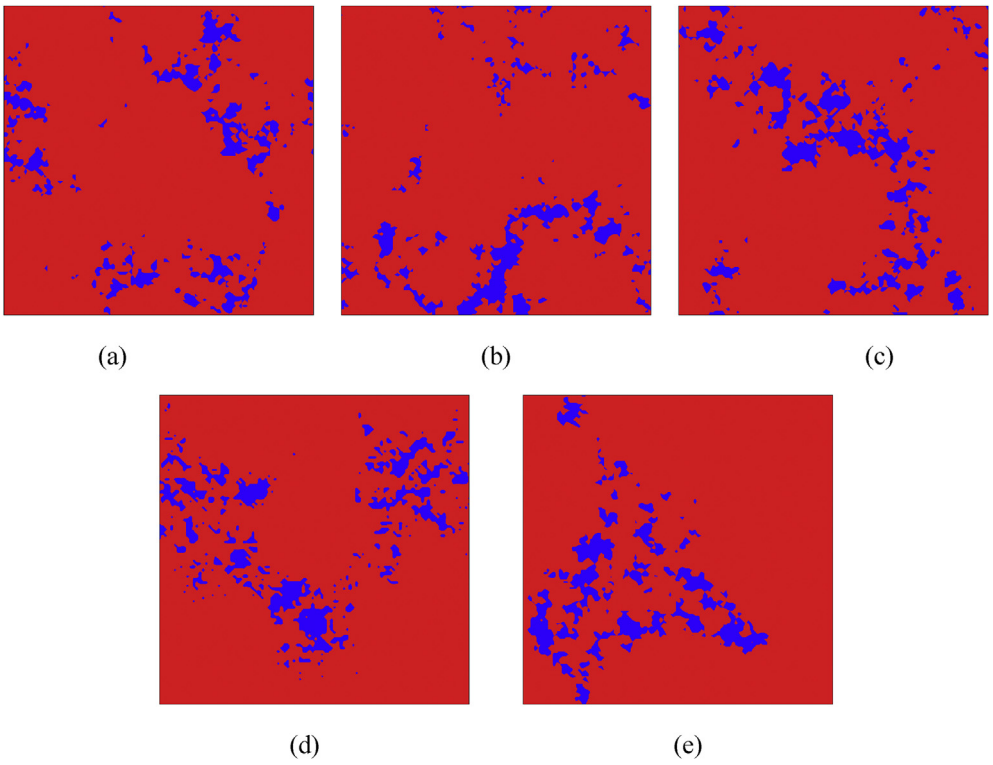

Fig. 10. The cross section of one group of the reconstructed heterogeneous structures, with pores represented by blue and matrix by red. The core distribution probability ratio from (a) to (e) is 100, 125, 167, 250, 500, respectively. (For interpretation of the references to colour in this figure legend, the reader is referred to the web version of this article.)

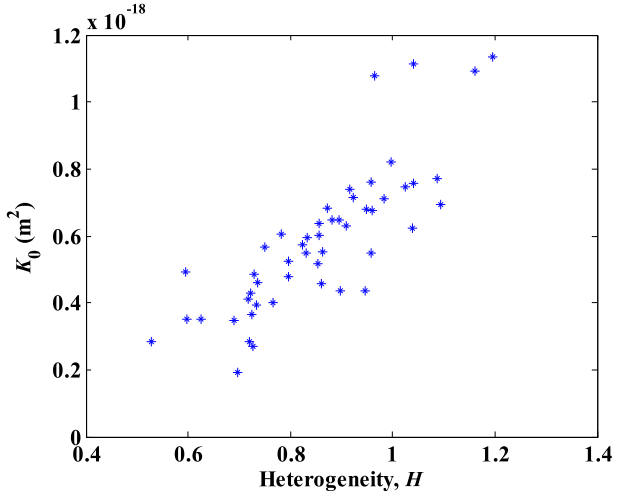

Fig. 11. The intrinsic permeability of structures with different heterogeneity, with each point reprenting the result of a reconstructed structure.

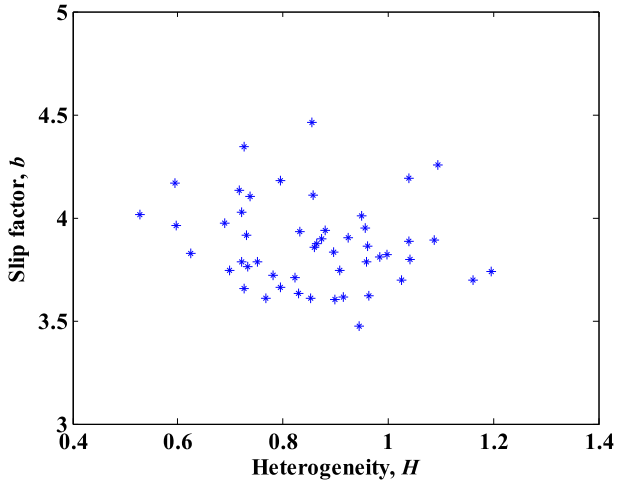

Fig. 12. The slip factor for heterogeneous structures, with each point reprenting a reconstructed structure.

parallel to the bed, which is the general case in shale. But for comparison, another set of structures are reconstructed to exam the permeability perpendicular to the bed. The parameters are consistent with Table 1 except the growth rate is $D_y = D_z = 0.008$; $D_z/D_x = 1,3,5,7,9$. It is well-known that for anisotropic structure, the parallel permeability is larger than the perpendicular permeability. In Fig. 8, we further show that the parallel permeability increases while perpendicular permeability decreases as anisotropy increasing. A possible explanation is that when anisotropy increases, the tortuosity in parallel direction increases while it decreases in perpendicular direction, as evidence shows that shale has much smaller tortuosity parallel to the bed (Revil et al., 2013).

Then the apparent permeability is predicted by introducing diffusive wall boundary condition and effective viscosity model in LBM. With the apparent permeability at a certain *Kn*, the slip factor is calculated as follows:

$$b = \frac{K/K_0 - 1}{Kn}, \tag{14}$$

where K is the apparent permeability and K_0 is the intrinsic permeability, both obtained through LBM simulation. As presented in Fig. 9 (a), when parallel to the bed, the slip factor increases with anisotropy, which means the high *Kn* effect is stronger in

anisotropic structures. This is because when shale gas flows through more wide but narrow pores, it is more likely to interact with the wall and the confining effect is more significant. However, in perpendicular direction the variation of slip factor is not as obvious, because shale has transversely isotropic structure and when the gas flowing along the symmetry axis, the pore geometry in the cross section is isotropic.

5.2. Heterogeneity

Similar to the study of anisotropy, we reconstruct ten groups of structures and each group has five structures with different heterogeneity. The parameters are listed in Table 2 and the cross sections of the structures are presented in Fig. 10. Heterogeneous pore distribution is obvious and the heterogeneity is positively related with the core distribution probability ratio c^R/c^C. The quantitative data of the averaged heterogeneity is given in Table 3, which is at the same level with real structure date in Table 1. But unlike anisotropy, the structures with same c^R/c^C are more dispersed in heterogeneity. The maximum and minimum heterogeneity of all the structures are 1.196 and 0.527 so the actual range of heterogeneity is much larger than presented in Table 3.

Fig. 11 presents the intrinsic permeability of all the reconstructed structures. It is clear that the intrinsic permeability increases rapidly with heterogeneity. When the heterogeneity is 0.6, the intrinsic permeability is around 0.3×10^{-18} m^2, while it increases to about 0.7×10^{-18} m^2 when heterogeneity reaches 1. Two main reasons are responsible for the increasing. First, at low heterogeneity the pores are more dispersed so it is more likely for a pore to be isolated (dead pore). After deleting the dead pores, the porosity drops from 10% to 8.90% for the structure with highest heterogeneity while to 8.05% for lowest heterogeneity. Second, the pores are better-connected when heterogeneity is high. When the pores are more concentrated, they have higher possibility to connect with others and narrow throats which can greatly constrain the flow are less likely to appear. Fig. 12 shows that the slip factor is not affected by the heterogeneity of the structure, which is expected because heterogeneity does not influence the pore geometry.

6. Conclusions

Shale permeability is much larger than the prediction of isotropic homogeneous models such as packed spheres or bundle of tubes. In this work, we investigate the influences of three pore-scale features of shale: anisotropic pore morphology, heterogeneous pore distribution and the dominant nanoscale pores. A quantification method for pore-scale anisotropy and heterogeneity is established and the permeability of reconstructed porous structure is predicted by high efficiency LBM. The following conclusions are obtained:

(1) The intrinsic permeability increases with the anisotropy of pore geometry in parallel direction to the bed, while decreases in perpendicular direction.
(2) For the same porosity, the intrinsic permeability is higher when the pore distribution is more heterogeneous.
(3) The high *Kn* effect is enhanced by pore-scale anisotropy when the gas flow is parallel to the bed.

Acknowledgements

This work is financially supported by the NSF grant of China (No. U1562217), National Science and Technology Major Project on Oil and Gas (No.2017ZX05013001), the PetroChina Innovation Foundation and the Tsinghua University Initiative Scientific Research Program (No. 2014z22074).

Appendix A

The link between the anisotropy defined by Eq. (1) and pore geometry is explained in this Appendix. Consider a 2D pore in a rectangular region. The width of the pore is w and the height is h; the size of the rectangle is $l_1 \times l_2$ (Fig. A1).

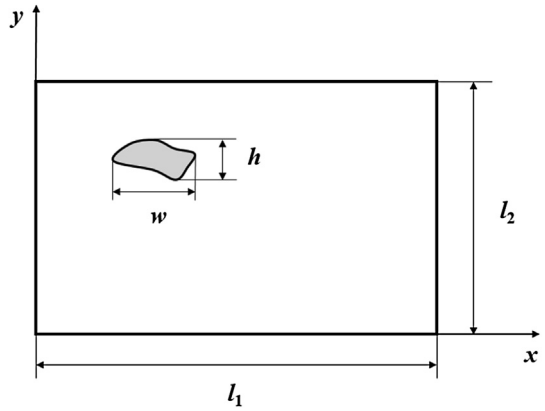

Fig. A1. The sketch for a pore with anisotropic geometry in the rectangular region.

Draw a line crossing the rectangle along x direction. The probability that it encounters the pore is h/l_2. Now consider that there are N pores in the rectangle and the width and height of each pore are w_i and h_i respectively, where $i = 1, 2, \ldots, N$. Then for the same line, the expectation of the total pore number it encounters is

$$N_x = \sum_{i=1}^{N} \frac{h_i}{l_2}. \tag{A1}$$

So the average pore number it can encounter per unit length is

$$n_x = \frac{N_x}{l_1} = \sum_{i=1}^{N} \frac{h_i}{l_1 l_2}. \tag{A2}$$

Similarly, in y direction we have

$$n_y = \sum_{i=1}^{N} \frac{w_i}{l_1 l_2}. \tag{A3}$$

So the anisotropy defined by Eq. (1) is

$$A = \frac{n_y}{n_x} = \left(\sum_{i=1}^{N} w_i\right) \Big/ \left(\sum_{i=1}^{N} h_i\right), \tag{A4}$$

which is the sum pore width over the sum of pore heights. If the aspect ratio $r = w/h$ is the same for each pore, the structure anisotropy equals to the pore aspect ratio, i.e. $A = r$. Otherwise, the anisotropy is the average aspect ratio with weight $h_i/\overline{h}$:

$$A = \sum_{i=1}^{N} \frac{r_i}{N} \frac{h_i}{\overline{h}}, \tag{A5}$$

where r_i is the aspect ratio for the i-th pore, $\overline{h}$ is the average pore height. This is expected because larger pores contribute more to the permeability so their influences should be stronger.

References

Ansumali, S., Karlin, I.V., 2002. Kinetic boundary conditions in the lattice Boltzmann method. Phys. Rev. E 66, 026311.

Begg, S.H., Chang, D.M., 1985. A Simple Statistical Method for Calculating the Effective Vertical Permeability of a Reservoir Containing Discontinuous Shales. Society of Petroleum Engineers.

Beskok, A., Karniadakis, G.E., 1999. A model for flows in channels, pipes, and ducts at micro and nano scales. Microscale Thermophys. Eng. 3, 43–77.

Bhandari, A.R., Flemings, P.B., Polito, P.J., Cronin, M.B., Bryant, S.L., 2015. Anisotropy and stress dependence of permeability in the Barnett shale. Transp. Porous Media 108, 393–411.

Burton, D., Wood, L.J., 2013. Geologically-based permeability anisotropy estimates for tidally-influenced reservoirs using quantitative shale data. Petrol. Geosci. 19, 3–20.

Chalmers, G.R., Bustin, R.M., Power, I.M., 2012. Characterization of gas shale pore systems by porosimetry, pycnometry, surface area, and field emission scanning electron microscopy/transmission electron microscopy image analyses: examples from the Barnett, Woodford, Haynesville, Marcellus, and Doig units. Aapg Bull. 96, 1099–1119.

Chen, S., Doolen, G.D., 1998. Lattice Boltzmann method for fluid flows. Annu. Rev. Fluid Mech. 30, 329–364.

Chen, L., Fang, W., Kang, Q., Hyman, J.D.H., Viswanathan, H.S., Tao, W.-Q., 2015. Generalized lattice Boltzmann model for flow through tight porous media with Klinkenberg's effect. Phys. Rev. E 91, 033004.

Civan, F., 2010. Effective correlation of apparent gas permeability in tight porous media. Transp. Porous Media 82, 375–384.

d'Humieres, D., Ginzburg, I., Krafczyk, M., Lallemand, P., Luo, L.S., 2002. Multiple-relaxation-time lattice Boltzmann models in three dimensions. Philos. Trans. R. Soc. Lond. Ser. A Math. Phys. Eng. Sci. 360, 437–451.

Gu, X., Cole, D.R., Rother, G., Mildner, D.F.R., Brantley, S.L., 2015. Pores in Marcellus shale: a neutron scattering and FIB-SEM Study. Energy & Fuels 29, 1295–1308.

Guo, Z.L., Zheng, C.G., Shi, B.C., 2002. Non-equilibrium extrapolation method for velocity and pressure boundary conditions in the lattice Boltzmann method. Chin. Phys. 11, 366–374.

He, X.Y., Luo, L.S., 1997. Theory of the lattice Boltzmann method: from the Boltzmann equation to the lattice Boltzmann equation. Phys. Rev. E 56, 6811–6817.

Higuera, F.J., Succi, S., Benzi, R., 1989. Lattice gas-dynamics with enhanced collisions. Europhys. Lett. 9, 345–349.

Kalarakis, A.N., Michalis, V.K., Skouras, E.D., Burganos, V.N., 2012. Mesoscopic simulation of rarefied flow in narrow channels and porous media. Transp. Porous Media 94, 385–398.

Kaluarachchi, J.J., 1995. Analytical solution to 2-dimensional axisymmetrical gas-flow with Klinkenberg effect. J. Environ. Eng. ASCE 121, 417–420.

Karniadakis, G., Beskok, A., Aluru, N., 2005. Microflows and Nanoflows. Springer, New York.

Klinkenberg, L.J., 1941. The permeability of porous media to liquids and gases, drilling and production practice. Am. Petrol. Inst. 200–213.

Knudsen, M.H.C., 1933. The Kinetic Theory of Gases; Some Modern Aspects. Methuen, London.

Kwon, O., Kronenberg, A.K., Gangi, A.F., Johnson, B., Herbert, B.E., 2004. Permeability of illite-bearing shale: 1. Anisotropy and effects of clay content and loading. J. Geophys. Res. Solid Earth 109, B10205.

Lallemand, P., Luo, L.S., 2000. Theory of the lattice Boltzmann method: dispersion, dissipation, isotropy, Galilean invariance, and stability. Phys. Rev. E 61, 6546–6562.

Lasseux, D., Jolly, P., Jannot, Y., Omnes, E.S.B., 2011. Permeability measurement of graphite compression packings. J. Press. Vessel Technol. Trans. ASME 133, 041401.

Lin, B., Chen, M., Jin, Y., Pang, H., 2015. Modeling pore size distribution of southern Sichuan shale gas reservoirs. J. Nat. Gas Sci. Eng. 26, 883–894.

Loucks, R.G., Reed, R.M., Ruppel, S.C., Jarvie, D.M., 2009. Morphology, genesis, and distribution of nanometer-scale pores in siliceous mudstones of the Mississippian Barnett shale. J. Sediment. Res. 79, 848–861.

McCarthy, J.F., 1991. Analytical models of the effective permeability of sand-shale reservoirs. Geophys. J. Int. 105, 513–527.

Pan, C., Luo, L.-S., Miller, C.T., 2006. An evaluation of lattice Boltzmann schemes for porous medium flow simulation. Comput. Fluids 35, 898–909.

Revil, A., Woodruff, W.F., Torres-Verdin, C., Prasad, M., 2013. Complex conductivity tensor of anisotropic hydrocarbon-bearing shales and mudrocks. Geophysics 78, D403–D418.

Sangani, A.S., Acrivos, A., 1982. Slow flow through a periodic array of spheres. Int. J. Multiph. Flow 8, 343–360.

Shmonov, V.M., Mal'kovskii, V.I., Zharikov, A.V., 2011. A technique for measuring permeability of samples of anisotropic rocks for water and gas. Instrum. Exp. Tech. 54, 722–728.

Tang, X., Jiang, Z., Li, Z., Gao, Z., Bai, Y., Zhao, S., Feng, J., 2015. The effect of the variation in material composition on the heterogeneous pore structure of high-maturity shale of the Silurian Longmaxi formation in the southeastern Sichuan Basin, China. J. Nat. Gas Sci. Eng. 23, 464–473.

Wan, Y., Pan, Z., Tang, S., Connell, L.D., Down, D.D., Camilleri, M., 2015. An experimental investigation of diffusivity and porosity anisotropy of a Chinese gas shale. J. Nat. Gas Sci. Eng. 23, 70–79.

Wang, Z.J., 2002. Seismic anisotropy in sedimentary rocks, part 2: laboratory data. Geophysics 67, 1423–1440.

Wang, M., Chen, S., 2007. Electroosmosis in homogeneously charged micro- and nanoscale random porous media. J. Colloid Interface Sci. 314, 264–273.

Wang, M.R., Kang, Q.J., 2009. Electrokinetic transport in microchannels with random roughness. Anal. Chem. 81, 2953–2961.

Wang, M., Pan, N., 2008. Predictions of effective physical properties of complex multiphase materials. Mater. Sci. Eng. R Rep. 63, 1–30.

Wang, M., Wang, J., Pan, N., Chen, S., 2007. Mesoscopic predictions of the effective thermal conductivity for microscale random porous media. Phys. Rev. E 75, 036702.

Wang, M., Pan, N., Wang, J.K., Chen, S.Y., 2007. Lattice Poisson-Boltzmann simulations of electroosmotic flows in charged anisotropic porous media. Commun. Comput. Phys. 2, 1055–1070.

Wang, M., Lan, X.D., Li, Z.X., 2008. Analyses of gas flows in micro- and nanochannels. Int. J. Heat Mass Transf. 51, 3630–3641.

Wang, Z., Guo, Y., Wang, M., 2016. Permeability of high-Kn real gas flow in shale and production prediction by pore-scale modeling. J. Nat. Gas Sci. Eng. 28, 328–337.

Zhang, P., Hu, L., Meegoda, J.N., Gao, S., 2015. Micro/nano-pore network analysis of gas flow in shale matrix. Sci. Rep. 5, 13501.